Journal of
Materials Chemistry A

Materials for energy and sustainability

Accepted Manuscript

This article can be cited before page numbers have been issued, to do this please use: K. Xu, J. Deng, R. Lin, H. Zhang, Q. Ke and C. Huang, *J. Mater. Chem. A*, 2020, DOI: 10.1039/D0TA07886G.

ROYAL SOCIETY OF CHEMISTRY

rsc.li/materials-a

View Article Online
DOI: 10.1039/D0TA07886G

ARTICLE

Surface Fibrillation of Para-aramid Nonwoven as a Multi-functional Air Filter with Ultralow Pressure Drop

Received 00th January 20xx,
Accepted 00th January 20xx

DOI: 10.1039/x0xx00000x

Kangli Xu[a], Jixia Deng[a], Rui Lin[b], Heng Zhang[c], Qinfei Ke*[a], and Chen Huang*[a]

Nonwovens are widely applied in air filtration field for their multi-layered fibrous structures and inter-connected pores. Despite intensively used, conventional microfiber nonwovens usually suffer from low filtration efficiencies due to their large pore size, whilst most nanofiber nonwovens are still confined within laboratory for the difficulties to reconcile the comprehensive requirements (such as low pressure drop, high fluffiness, strength and long-term reliability) raised from practical applications. Here we report a simple and scalable method that can generate lots of nanofibrils in a para-aramid microfiber nonwoven without interfering the three-dimensional nonwoven structure. The success of this method relies on treating the whole nonwoven, rather than individual fibers, with phosphoric acid to trigger a surface fibrillation process of para-aramid microfibers. The structural reinforcement from microfibers, in combination with the enlarged surface area and the reduced pore size brought by nanofibrils, improves the filtration efficiency of fibrillated nonwoven by 84.7% and maintains the pressure drop at an ultralow value of 3.5 Pa. Further synthesis and loading of a novel catalyst (CuO-CeO_2) onto the nonwoven demonstrate a higher catalyst-loading capacity after fibrillation. The resulting nonwoven filter shows high elimination rates against a variety of solid and gaseous pollutants (including particulate matters, carbon monoxide and toluene), and is applicable under both room and elevated temperature. We believe that the generation of nanofibrils in microfiber nonwoven and the subsequent loading of catalysts will find extensive utility in the purification of industrial emissions, automobile exhausts and indoor air.

Introduction

Air pollution caused by industrial and vehicular emissions has becoming one of the most severe threats to public health, climate and ecosystems.[1-5] The major contaminants in polluted air are divided into two categories: particulate matters (PMs) and toxic gases.[6-9] PMs refer to the solid particles and aerosols with diameters no more than 10 μm, and toxic gases are the generic term of carbon monoxide (CO), sulfur oxides (SO_x), nitrogen oxides (NO_x), ammonia (NH_3), hydrocarbons and volatile organic compounds (VOCs).[10-12] Given that the exposure to PMs and toxic gases may drastically increase the risks for respiratory, skin and cardiovascular diseases,[13-15] the design and development of air filtration systems have drawn increasing interests from both industry and academia.

Till now, microfiber nonwovens manufactured by needle-punch, meltblown and spunbond technologies are the most successful media for constructing air filters. These nonwovens are featured with large scale and low-cost production, multiple layers of fibers and interconnected porous structures, leading to both good filtration performances and desirable practicability.[16-20] However, since conventional nonwovens can only remove PMs with a relatively low efficiency, additional layers of materials (such as microporous films and active carbon) or post-treatments (such as electret) are frequently applied.

To address the low filtration efficiency of microfiber nonwovens, nanofibers with diameter ranging from tens to hundreds of nanometers have emerged as promising building blocks for high efficiency nonwoven filters. The concept of using nanofiber nonwovens as air filters is established by the fact that filtration efficiency of air filters can be readily improved through reducing pore size, while pore size of nonwovens is positively correlated to fiber diameter. For this reason, a number of nanofiber nonwovens with delicate architecture have been fabricated. Some representative works include the microwave structured polyamide-6/poly(m-phenylene isophthalamide) nanofiber/net membranes,[21] the self-assembled 2D nanoarchitectured networks,[22] the mesostructured nonwovens with penguin downy feather-like morphology,[23] and the bead-on-string polyacrylonitrile nanofibrous air filters.[24] All of them possessed ideal filtration efficiencies.

In spite of the exciting progresses these studies have made, the practical use of nanofiber nonwovens in air filtration is still largely confined within laboratory, due to the intrinsic conflict between high filtration efficiency and low pressure drop. While the small pore size of nanofiber nonwoven is desirable for increasing filtration

[a] Key Laboratory of Textile Science & Technology, Ministry of Education, College of Textiles, Donghua University, Shanghai 201620, China. E-mail: hc@dhu.edu.cn kqf@dhu.edu.cn
[b] Laboratory of Clean Energy Utilization and Pollution Control, College of Environmental Science and Engineering, Donghua University, Shanghai 201620, China.
[c] State Key Lab High Performance Ceram & Superfine, Shanghai Institute of Ceramics, Chinese Academy of Sciences, Shanghai 200050, China.
† Electronic Supplementary Information (ESI) available: Experimental details, XRD patterns, FTIR spectrum, TGA curves, photographs of CuO-CeO_2/fibrillated para-aramid nonwoven. See DOI: 10.1039/x0xx00000x

View Article Online
DOI: 10.1039/D0TA07886G

efficiency, it may easily cause the sharp increase of pressure drop. Although some recent work tried to tackle the problem by constructing three-dimensional (3D) architectures[25-26] or utilizing the "slippery effect" of nanomaterials,[27-28] the reported pressure drops are still higher than those of the microfiber nonwovens. Moreover, when used under harsh environment (which is commonly occurred in industrial air filtration), strength and long-term reliability of nanofiber nonwovens remain to be verified, since these delicate structures are highly vulnerable to high-flux air flow and chemical corrosion. The development of next generation of air filters has, therefore, turned to the design and fabrication of nonwovens with new and multiscale fiber morphologies.

Herein we present a nonwoven air filter having ultralow pressure drop and efficient removal rates to both PMs and toxic gases. By treating a conventional para-aramid microfiber nonwoven with phosphoric acid (H_3PO_4) aqueous vortex, we successfully activate the surface fibrillation of the microfibers and generate a large number of nanofibrils on fiber surface. The co-existence of microfibers and nanofibers endows the fibrillated nonwoven with stable 3D structure, reduced pore size and enlarged surface area, which work synergistically to achieve excellent filtration performances that outperform other known fibrous filters of similar dimensions or origins. When loaded with a novel catalyst ($CuO\text{-}CeO_2$), the nanofibrils greatly increase the loading capacity of the nonwoven, and thus enabling an improved elimination rate against toxic gases such as CO and toluene (C_7H_8). The high reliability of resulting nonwoven was further verified by a series of stability tests, including compression resilience, adhesion fastness, thermal and chemical stabilities. These results prove the efficacy of using fibrillated para-aramid nonwoven in air filtration, especially when encountering harsh working environments and different types of airborne pollutants.

Experimental

Materials

Para-aramid fiber (Kevlar 29, diameter ~14 μm) was supplied by Dupont (U.S.A). Phosphoric acid (≥85.0%, H_3PO_4), cerous nitrate hexahydrate (≥99.0%, $Ce(NO_3)_3{\cdot}6H_2O$), copper(II) nitrate trihydrate (≥99.0%, $Cu(NO_3)_2{\cdot}3H_2O$), formic acid (≥98.0%, HCOOH), and sodium hydroxide (≥99.0%, NaOH) were purchased from Sinopharm Chemical Reagent Co., Ltd. Hexadecyl trimethyl ammonium bromide (≥99.0%, CTAB) was purchased from Aladdin Chemical Reagent Co., Ltd. Ammonia (25%, NH_3) was purchased from Lingfeng Chemical Reagent Co., Ltd. All chemicals were used without further purification.

Surface fibrillation of para-aramid microfiber nonwoven

Para-aramid nonwoven was manufactured *via* an industrialized web forming (carding) and bonding (needle punching) process. Para-aramid fibers were fed into a carding machine to produce uniform fiber webs. The webs (areal density = 200 $g{\cdot}m^{-2}$) were then overlapped and needle punched with a puncturing density of 600 $punch{\cdot}cm^{-2}$. The bonded para-aramid nonwoven was cleaned in mixed solution of acetone and ethanol to remove the surface oils. After drying in a vacuum oven at 60 ℃ for 6 h, the nonwoven was impregnated in different concentrations of H_3PO_4 solution (10%, 20%, 30%, 40% and 50%) and stirred for 1 h, 2 h, 3 h and 4 h, respectively. The stirring speed was set at 600 rpm, and the water bath temperature was 55 ℃. Under the shearing force of H_3PO_4 solution, nanofibrils were stripped from the surface of para-aramid fibers, after that the para-aramid nonwoven was washed with deionized water for 3 times and dried in a vacuum oven at 60 ℃ for 12 h.

Synthesis and loading of $CuO\text{-}CeO_2$

A series of $CuO\text{-}CeO_2$ catalysts were synthesized by a hydrothermal method.[29] 1 g CTAB was dissolved in 50 mL of distilled water under constant stirring. $Cu(NO_3)_2{\cdot}3H_2O$ and $Ce(NO_3)_3{\cdot}6H_2O$ of different molar ratios (5/95, 10/90, 15/85) were added into the above solution as precursor salts. NH_3 aqueous solution was added dropwise with stirring at 50 ℃ until the pH value of the mixture was adjusted to 10.0. The solution was transferred to a 100 mL Teflon-line stainless steel autoclave for hydrothermal reaction at 160 ℃ for 12 h. The resulting products were sequentially cooled down to room temperature, washed fully *via* deionized water and ethanol, dried under vacuum at 60 ℃ for 24 h, and calcined at 500 ℃ for 2 h in air. The resultant samples were named as *x* $CuO\text{-}CeO_2$, where *x* denotes the molar percentage of Cu in the catalysts.

At the concentration of 0.2 wt%, a uniform and stable $CuO\text{-}CeO_2$ dispersion is formed under ultrasonication. The fibrillated para-aramid nonwoven was impregnated in this dispersion for another 30 min of continuous ultrasonication, after which it was washed by deionized water to remove the floating particles, and dried in a vacuum at 110 ℃ for 12 h.

Characterization

Surface morphology of samples was detected by field emission scanning electron microscope (FESEM, Hitachi S-4800, JEOL, Japan) coupled with an energy-dispersive spectrometry (EDS). Transmission electron microscopy (TEM, JEM-2 011F, JEOL, Japan) was performed at an accelerating voltage of 200 kV. Crystalline structures of the samples were characterized by X-ray diffraction (XRD, D/max-II B, Shimadzu, Japan). CuKα1 radiation of 1.54056Å and graphite monochromator (40 kV, 30 mA) were used with a step size of $5°{\cdot}min^{-1}$ in the range from 5 to 90°. The basis weight and thickness of nonwovens were determined using an electronic balance and a thickness gauge. The compression tests were conducted using compression apparatus equipped with two flat-surface compression stages (INSTRON 5967, U.S.A). Ten samples of the same size (30 × 30 mm) were stacked together for the compression test. A 100-cycle loading–unloading fatigue test was performed by measuring σ versus ε = 53% at a strain rate of 5 $mm{\cdot}min^{-1}$ and a 3% prestrain was applied to ensure a uniform flat contact between the presser foot and the samples.[30] The stress-strain curves were acquired with an electronic fabric tensile device (YG026MB, China) at a speed of 10 mm/min. Raman spectra were acquired by using a Raman system (inVia-Reflex, U.K.) with 532 nm excitation. Fourier transform infrared spectroscopy (FT-IR, Spectrum Two, U.K.) was used to investigate the functional groups of the samples at the wavenumber ranging from

View Article Online
DOI: 10.1039/D0TA07886G

4000 to 400 cm^{-1}. Water contact angle (WCA) was measured by a contact angle goniometer (OCA15EC, Germany). Thermo gravimetric analysis (TGA) was conducted by TGA-4000 (PerkinElmer, Netherlands), and the temperature was increased from 30 to 700 ℃ at 20 ℃·min^{-1}. Flame retardancy properties were visualized *via* a combustion test using an alcohol lamp. Nitrogen adsorption-desorption isotherms were measured at 77K using a micromeritics ASAP 2460 analyzer (Micromeritics Instruments, U.S.A). The specific surface area (SSA) were calculated by Brunauer-Emmett-Teller (BET) method, using the adsorption branch data in the relative pressure (P/P_0) ranging from 0.0 to 1.0. Pore volumes of catalysts were calculated by the t-plot method, and pore size distribution of catalysts was calculated by Barrett-Joyner-Halenda (BJH) method using nitrogen desorption branch data. Pore size and pore size distribution of para-aramid nonwovens were measured by a capillary flow porometer (CFP-1100AI, Porous Materials, Inc., U.S.A). Inductively coupled plasma atomic emission spectroscopy (ICP, Prodigy, U.S.A) was carried out to measure the actual elemental contents and compositions of the catalysts.

A PH15700 ESCA X-ray photoelectron spectroscopy instrument (XPS, Thermo Fisher Scientific Inc., U.S.A) was employed to check the chemical states of Ce and Cu in the catalysts by using Al-Kα (Eb = 1486.6 eV) radiation with an accelerating voltage of 15 kV. The percentages of surface atoms of the elements in catalysts were calculated by the areas of the binding energy after correction and normalization. The organic polluted carbon (C1s: E = 284.6 eV) was used as the corrective standard of energy.

TPR experiments were performed on gas chromatograph (GC-4000A, U.S.A) equipped with thermal conductivity detector (TCD). The heating range of the whole reduction process was from 50 to 600 ℃ (5 ℃·min^{-1}) and was tested in 5% H_2/N_2 (20 mL·min^{-1}) atmosphere. Catalyst samples were crushed through a 40-60 mesh sieve and loaded into the reaction quartz tube. Before the test, catalyst samples were heated from 30 to 300 ℃ (5 ℃·min^{-1}) in N_2 environment, and maintained at 300 ℃ for 30 min.[31]

Two methods were adopted to examine the dry and wet adhesion fastness of $CuO\text{-}CeO_2$ particles on fibrillated nonwoven. One is continuous air blowing at 5 m·s^{-1} for 10 min (sample size = 30 × 20 cm), the other is washing under 1000 r·min^{-1} for 10 min (sample size = 2 × 2 cm). After 3 cycles of air blowing or washing, the nonwoven was taken out and dried in a vacuum oven at 60 ℃ for 12 h. The weight of the nonwoven before and after air blowing/washing were recorded. Chemical stability of $CuO\text{-}CeO_2$/fibrillated nonwoven was investigated by immersing the nonwoven in 98% HCOOH solution and 0.5 mol·L^{-1} NaOH solution for 1 h,[32] after which the filtration performances of the nonwovens were measured.

Filtration tests

The filtration tests were conducted by following European Standard of Medium Efficiency Filters (BS EN 779:2012). A CertiTest 8130 automatic filtration performance tester (TSI Inc., U.S.A) was used and the air flow was set at 32 L·min^{-1}. Solid sodium chloride (NaCl, 2wt%) was employed to generate particles (mean diameter ~0.26 μm and the geometric standard deviation of the particles was less than 1.83). NaCl aerosol particles were delivered through the filter, which were clamped by a filter holder with an effective area of 100 cm^2. Before testing, the aerosol generator was preheated for more than 30 min to ensure the accuracy of data. The filtration efficiency (η) could be calculated as follow:

$$\eta\ (\%) = (1 - \varepsilon_1/\varepsilon_2) \times 100\% \qquad (1)$$

where ε_1 and ε_2 represent the quantity of NaCl aerosol in the downstream and upstream, respectively. Pressure drop (filtration resistance) was recorded by a flow gauge and two electronical pressure transmitters.

Catalytic activity tests

The catalytic oxidation of CO was carried out in a self-developed fixed-bed reactor system under atmospheric pressure (Figure S1). 100 mg of pure catalyst (40-60 mesh) or 0.5 g of catalyst-loaded nonwoven were heated from 30 to 240 ℃ with a rate of 5 ℃·min^{-1}. The typical composition of feed gas mixture comprises CO (1 %), O_2 (10 %) and N_2 (to balance), and the total flow rate was fixed at 200 mL·min^{-1} to ensure a gas hourly space velocity (GHSV) of 120000 mL (g_{cat}·h^{-1}).[33] The inlet and outlet concentrations of reactants and products were measured by an on-line GC equipped with a TCD, a flame ionization detector and a methanation reactor. The reaction gas and products were separated by TDX-1 columnar molecular sieve, and the conversion rate was calculated by area normalization method. The catalytic activities were expressed according to the conversion of CO (%), which was calculated based on the consumptions of CO:

$$\text{CO conversion (\%)} = \frac{[CO]_{in} - [CO]_{out}}{[CO]_{in}} \times 100\% \qquad (2)$$

where $[CO]_{in}$ and $[CO]_{out}$ are the concentrations of CO (%) in the feed stream and the effluent, respectively.

Another important indicator for evaluating the catalyst is the stability of catalyst. This test was also carried out in a tubular continuous reactor, and the test conditions are the same as those for CO oxidation. In the life test, the samples were kept at 90 ℃ (which is the lowest temperature for 100% CO conversion) for 1200 min and the change of conversion rate was recorded during the test period.

Adsorption and photodegradation test.

The photodegradation tests were carried out in a reactor (1.0 μL) at a standard atmospheric pressure and room temperature (Figure S2). 100 mg of $CuO\text{-}CeO_2$ or 0.5 g of $CuO\text{-}CeO_2$-loaded nonwoven were placed in the reactor. The atmosphere of the reactor is the same as the indoor environment. After the baseline became stable, 1.0 μL toluene were injected into the reactor by a liquid injector needle, and the corresponding initial concentration was 867 mg·m^{-3}. After C_7H_8 vapor reached adsorption equilibrium, the photocatalytic activity tests were performed under xenon lamp irradiation (300 W, PLSSXE300, Beijing philae technology co., Ltd., China). The concentrations of C_7H_8 and CO_2 in the reactor were determined online by a photoacoustic gas monitor (INNOVA 1412i, LumaSense Technologies, Denmark). The photocatalytic oxidation efficiencies of C_7H_8 into CO_2 ($\eta_{t,\ C_7H_8}$) were calculated according to the following formulas:

$$\eta_{t,\ C_7H_8}\ (\%) = 1 - \frac{\left(C_{t,CO_2} - C_{0,CO_2}\right) \cdot M_{C_7H_8}}{7C_{0,C_7H_8} \cdot M_{CO_2}} \times 100\% \qquad (3)$$

View Article Online
DOI: 10.1039/D0TA07886C

Where $C_{0,CO2}$ and $C_{0,C7H8}$ are the initial concentrations of CO_2 and C_7H_8, $C_{t,CO2}$ is the concentrations of CO_2 at time (t), and M_{C7H8} and M_{CO2} are the molecular weights of CO_2 and C_7H_8.

Results and discussion

Different from previous fibrillation methods that all using fibers as objects,[34-37] our strategy is based on nonwoven rather than individual fibers. As illustrated in Scheme 1, para-aramid nonwoven with the thickness of 1.8 mm was first produced by subjecting para-aramid microfibers to a typical web forming (carding) and bonding (needle punching) process. The surface fibrillation process was then triggered by immersing the nonwoven in H_3PO_4 solution under vigorous stirring. Due to the joint effects of chemical hydrolysis and physical shearing, the transverse intermolecular forces at the surface of para-aramid microfibers were weakened, resulting in the generation of nanofibrils. H_3PO_4 was selected for its moderate fibrillation effect, and the degree of fibrillation was adjusted by the concentration of H_3PO_4 and the reaction time. With inadequate concentration or time, the generation of nanofibrils is insufficient, whereas an excessive concentration or time would result in complete collapse of microfibers into nanofibrils. After comprehensively comparing fiber morphology, mechanical properties and filtration performances of fibrillated nonwovens (Figure S4), we set the optimal concentration at 30% and the reaction time at 3 h. Note here that other acids, such as sulfuric acid (H_2SO_4) and acetic acid (CH_3COOH) were also used for fibrillation, and the pH values of H_2SO_4, H_3PO_4 and CH_3COOH under the same concentration (30%) are -1.15, 0.25 and 1.92, respectively. The results (Figure S3) show that solution of low pH would cause fast and excessive decomposition of microfiber, while solution of high pH requires a much longer fibrillation time. The shearing effect on fibrillation process was also analyzed by changing the stirring speed. The results (Figure S5) show that with the increase of stirring speed, both the number and the length of nanofibers increased. However, when the stirring speed reaches 900 rpm, the strong shearing force would start to destroy the crystal structure of fiber core, which may cause the decrease of nonwoven strength. Therefore, we used a moderate stirring speed of 500 rpm in the following experiments. As shown in Figure 1a, the acquired nonwoven exhibits a distinct 3D structure, with microfibers serving as the primary structure, and surrounding nanofibrils as the secondary structure.

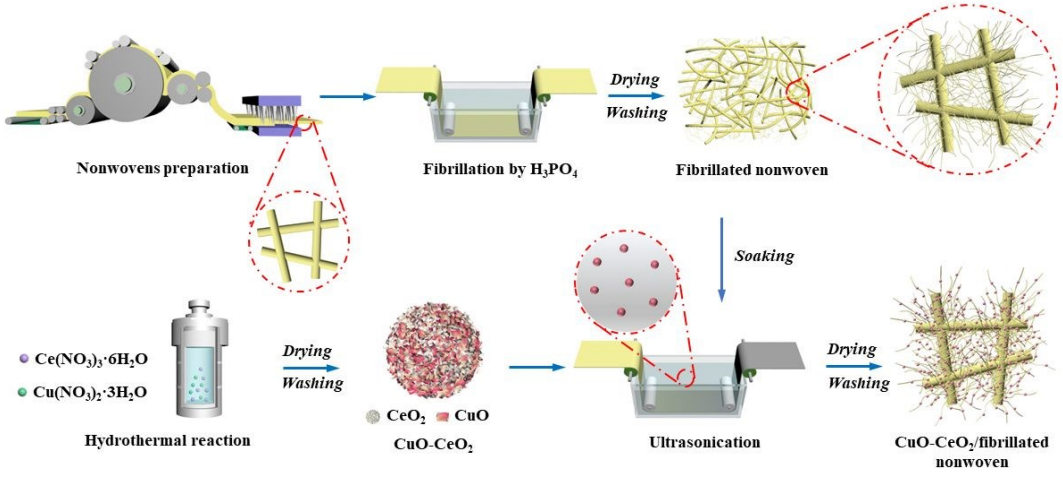

Scheme 1. Schematic illustration of fabrication, fibrillation and catalyst-loading of 3D para-aramid nonwoven.

In comparison to the pristine nonwoven (Figure 1b), the fibrillated nonwoven shows no change in dimension or color when observed from the macroscopic view. This indicates that the surface fibrillation process holds no interference on the 3D fluffy structure of microfiber nonwoven. To the best of our knowledge, this is the first report of 3D para-aramid nonwoven generated by fibrillation, for that previous methods all resulted in 2D nanofibrous membranes.[38-40] The smooth microfibers become rougher after fibrillation, and the large interfiber pores are filled with numerous nanofibrils, leading to a notable decrease of pore size from 36.3 to 18.9 μm (Figure 1c). Considering that the highly fluffy, 3D nonwoven architecture remains unchanged, we speculate that the reduction of pore size may have positive impacts on the filtration performances. To validate our assumption, air filtration tests were conducted by strictly following the procedure from European Standard of Medium Efficiency Filters (BS EN 779:2012). According to the results in Figure 1d, the fibrillated nonwoven shows a significantly improved filtration efficiency of 84.7% (twice that of pristine nonwoven) and an ultralow pressure drop of 3.5 Pa, making the quality factor (QF), a trade-off parameter between average filtration efficiency (η) and average pressure drop (ΔP) that reflects the overall filtration performances of filter,[41] increases significantly from 0.150 to 0.536 Pa^{-1}. This value is superior to many of the state-of-art fiber filters (Figure S6),[16, 42-46] and the pressure drop is far less than the requirements in the Standard. Here the low pressure drop is mainly ascribed to that the nanofibrils on the surface of microfibers do not overlap to form a fixed network structure, and the pore size of fibrillated nonwoven is still large, which has no obvious blocking effect on the passing airflow. Moreover, under the action of air flow, nanofibers that are originally attached to the surface of microfibers may float into the air to form a brush-like structure. Since the air velocity is nonzero at the fiber surface, the momentum of PMs makes them easily collide with the nanofibers when passing through nonwoven. In addition, these nanofibers possess more active sites and stronger adsorption capacity than microfibers because of their higher interface energy. Therefore, the diffusion and interception effects for PM capture are

View Article Online
DOI: 10.1039/D0TA07886G

greatly enhanced, leading to an improved filtration efficiency. The above mechanism is further verified by using NaCl particles to mimic the PMs. As shown in Figure S7, the nanofibers captured much more particles than the microfibers.

The impacts of H_3PO_4 treatment on the microstructure of para-aramid fibers were analyzed by X-ray diffraction (XRD) and thermogravimetry analysis (TGA). The curves before and after fibrillation are highly comparable (Figure S8), implying that both crystallinity and thermal behavior of para-aramid fibers are not altered. Moreover, owning to the support from microfibers, the 3D structure of fibrillated nonwoven remains intact after 100 cycles of repeated compression (Figure 1e), and the tensile stress of fibrillated nonwoven is still up to 11.4 MPa (inset of Figure 1e).

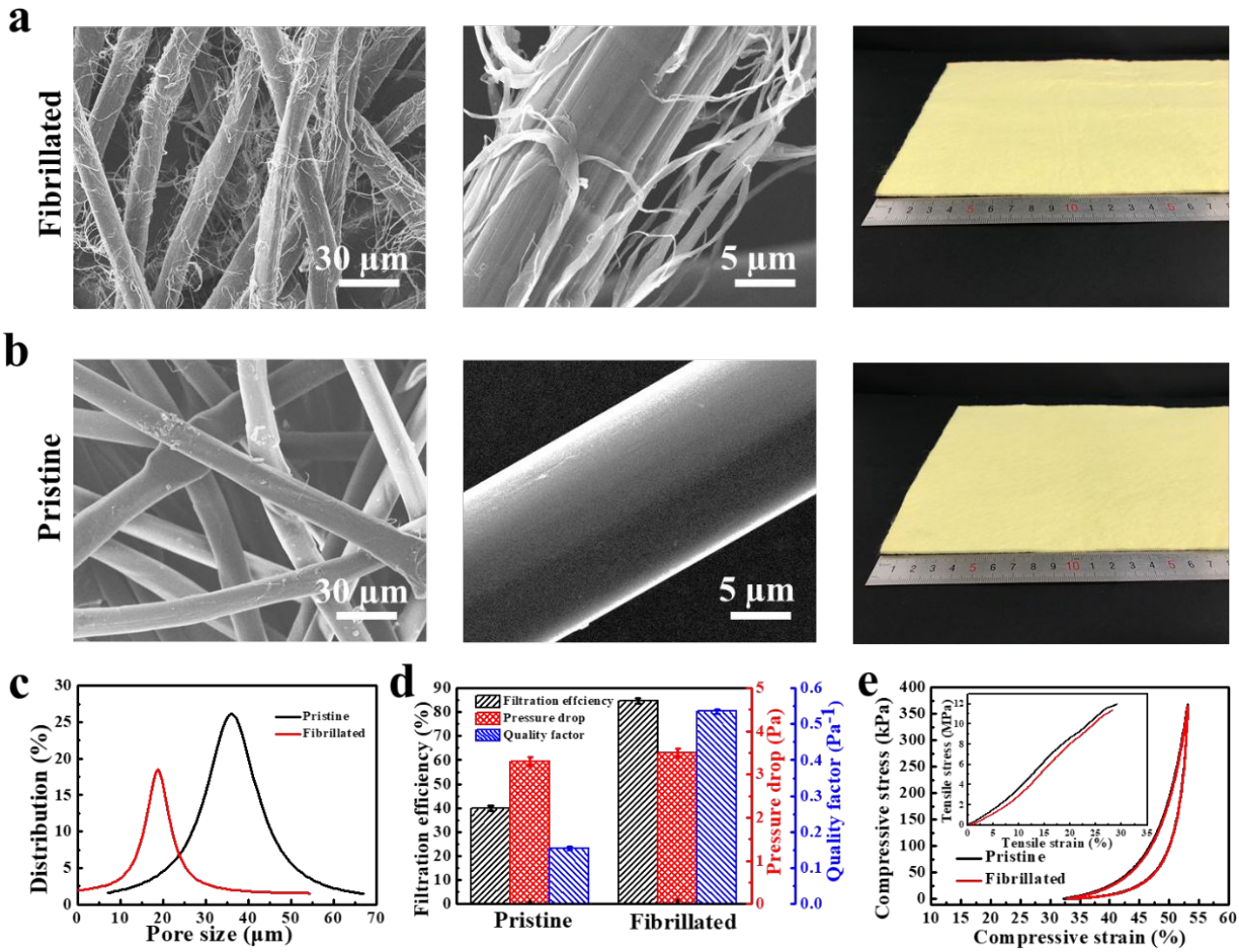

Figure 1. SEM images and digital photos of (a) fibrillated para-aramid nonwoven and (b) pristine para-aramid nonwoven. (c) Pore size distribution, (d) filtration performances, and (e) compressional resilience and tensile stress of pristine and fibrillated para-aramid nonwovens.

Besides decreasing pore size, the generation of nanofibrils holds another advantage in increasing the SSA. According to Brunauer-Emmett-Teller (BET) method, SSA of para-aramid nonwovens before and after fibrillation are 0.6 $m^2 \cdot g^{-1}$ and 12.3 $m^2 \cdot g^{-1}$, whilst pore volume of nonwovens before and after fibrillation are 0.0002 $cm^3 \cdot g^{-1}$ and 0.0035 $cm^3 \cdot g^{-1}$, respectively (Figure S9). Such a sharp increase in surface area and pore volume makes us hypothesize that, when used as carrier for catalysts, the fibrillated nonwoven may possess a high loading capacity, which is favorable for eliminating toxic gases from polluted air. To this end, we synthesized a group of CuO-CeO_2 catalysts by mixing $Ce(NO_3)_3 \cdot 6H_2O$, $Cu(NO_3)_2 \cdot 3H_2O$ and ammonia in a high-pressure reactor for hydrothermal reaction. CeO_2 was employed as the promoter of catalyst for its excellent stability, oxygen mobility and promotion of metal dispersion.[47-48] The morphology analyses of CeO_2 suggest that flower-like CeO_2 particles with an average size of 250 nm has the largest surface area and the highest CO oxidative activity (Figure S10 and Table S1). We therefore introduced CuO onto the flower-like CeO_2, with the aim to generate more oxygen vacancies (CeO_2–x) and increase the oxidation capacity of catalysts.[49] The ratio of Cu in final products (CuO-CeO_2) was confirmed by inductively coupled plasma (ICP) analysis (Table S2), and the optimal molar percentage of Cu was determined by comparing catalytic performances of different CuO-CeO_2. As shown in Figure 2a-c, increasing Cu content makes the particle size of CuO-CeO_2 larger, and the petal of flower-like structure becomes more apparent. The (111) crystal facets of CeO_2 are found in the high-resolution transmission electron microscope (HRTEM) images of all samples, suggesting that the addition of CuO has no damage to the flower-like structure.[50] Here we find that the (002) crystal facets of CuO only exist in samples containing 15% CuO, whereas Cu is found

in the line-scan energy-dispersive spectrometry (EDS) of every sample. This indicates that at low proportion (i.e. ≤10%), the CuO particles are highly dispersed and uniformly distributed on the surface of CeO_2, whereas particle aggregation would become inevitable if the proportion of CuO gets higher. More evidence can be found in X-ray diffraction (XRD) patterns (Figure S11), where characteristic peaks of CuO are detected when the ratio gets higher than 10%. Chemical states of Ce, Cu and O were further analyzed by fitting the spectra of Ce3d, Cu2p and O1s *via* a peak division method described previously.[51-53] According to Figure 2d, in Ce3d spectra, u' and v' peaks are associated with Ce^{3+}, and the other six peaks are ascribed to Ce^{4+}.[47] The presence of Ce^{3+} represents the existence of oxygen vacancies, which can facilitate the oxidation of toxic gases (CO in particular).[51] In Cu2p spectra, the lower ratio of shake-up satellite to the main peak of $Cu2p_{3/2}$ (nominated as I_{sat}/I_{main}) corresponds to a higher amount of reduced Cu species.[54] This is also conducive to the oxidation of CO, as the interaction between reduced Cu species with Ce was the main active site for CO oxidation.[55-56] In O1s spectra, the peaks at 529.3 eV and 531.6 eV correspond to the lattice oxygen (O_{latt}) species and surface hydroxyl groups (O_{OH}), respectively, and O_{OH} has been reported as the most active oxygen in oxidation reactions.[29] As summarized in Table 1, the optimal ratios of $Ce^{3+}/(Ce^{4+} + Ce^{3+})$, I_{sat}/I_{main} and $O_{OH}/(O_{latt} + O_{OH})$ are all achieved at the CuO proportion of 10%, which suggests in theory that when CuO is introduced, the catalytic activity of CuO-CeO_2 would increase first, but then decrease when the content of CuO exceeds 10%. This trend is confirmed by hydrogen temperature programmed reduction (H_2-TPR) and CO conversion tests. H_2 reduction profile demonstrates that the reduction temperature of H_2 is decreased due to the combination of CuO and CeO_2.[57] The minimum temperature for converting CO is also reduced with the presence of CuO (Figure S12). Among the CuO-CeO_2 catalysts, the lowest temperature (peak α) reducing H_2 is acquired by 0.10 CuO-CeO_2 (Figure 2e), and the complete conversion of CO by 0.10 CuO-CeO_2 is achieved at 90 ℃, which is at least 30 ℃ lower than using 0.05 CuO-CeO_2 and 0.15 CuO-CeO_2 (Figure 2f). The reliability of 0.10 CuO-CeO_2 catalyst is further demonstrated by a time-on-stream (TOS) test of 1,200 min, during which no significant changes in the conversion of CO is observed (Figure 2g). In consistence to the HRTEM results, these findings prove that the Cu species are uniformly dispersed and in close contact with Ce. When more Cu species enter the lattice of Ce, additional Ce^{3+} and oxygen vacancies would be created ($Cu^{1+}+Ce^{4+}\leftrightarrow Cu^{2+}+Ce^{3+}$) for oxidizing CO.[58-60] As the proportion of CuO keeps increasing, however, the CuO particles intend to aggregate and form CuO bulks, which would largely weaken the conversion capacity of catalysts.[61]

View Article Online
DOI: 10.1039/D0TA07886G

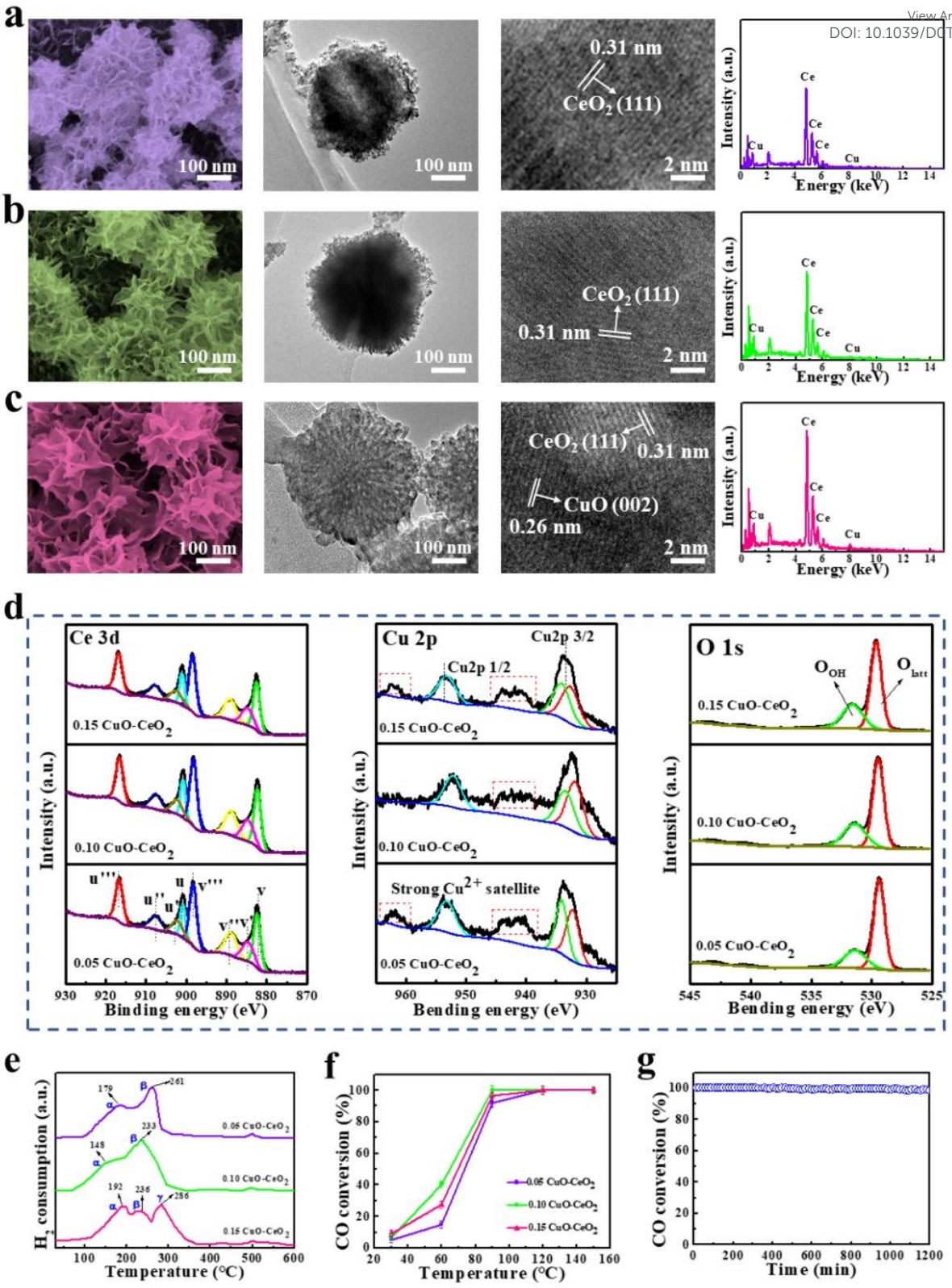

Figure 2. SEM images, TEM images, corresponding HRTEM images and EDS spectrum of (a) 0.05 CuO-CeO_2, (b) 0.10 CuO-CeO_2 and (c) 0.15 CuO-CeO_2. (d) XPS spectra of Ce3d, Cu2p and O1s for 0.05 CuO-CeO_2, 0.10 CuO-CeO_2 and 0.15 CuO-CeO_2. (e) H_2-TPD and (f) CO conversion of 0.05 CuO-CeO_2, 0.10 CuO-CeO_2 and 0.15 CuO-CeO_2. (g) Stability test of 0.10 CuO-CeO_2 for 1,200 min.

View Article Online
DOI: 10.1039/D0TA07886G

Table 1. Textural properties of $CuO\text{-}CeO_2$ catalysts with different molar percentages of Cu.

Samples	$Ce^{3+}/(Ce^{4+}+Ce^{3+})$ [%]	I_{sat}/I_{main} [%]	$O_{OH}/(O_{latt}+O_{OH})$ [%]
0.05 $CuO\text{-}CeO_2$	17.53	33.23	28.32
0.10 $CuO\text{-}CeO_2$	18.26	26.45	33.43
0.15 $CuO\text{-}CeO_2$	18.11	29.37	33.16

We then incorporated 0.10 $CuO\text{-}CeO_2$ catalysts on the para-aramid nonwovens *via* ultrasonic impregnation (Scheme 1). SEM images (Figure 3a) and energy dispersive X-ray analysis (EDX, Figure 3b) show the homogenous distribution of $CuO\text{-}CeO_2$ in both fibrillated and pristine nonwovens, whereas in fibrillated nonwovens, the $CuO\text{-}CeO_2$ particles are found on the surfaces of both microfibers and nanofibrils, leading to a much stronger intensities of Ce, Cu and O. This verifies that the existence of abundant nanofibrils can provide more adhesion sites for catalysts. More distinct difference of loading capacities is visualized by digital photos (Figure S13), the fibrillated nonwoven shows a darker and more evenly distributed black color than the pristine nonwoven. The actual loading capacities of two nonwovens were further quantified *via* thermo gravimetric analysis (TGA) (Figure 3c). Para-aramid fibers start to decompose at 540 °C, while $CuO\text{-}CeO_2$, as a type of inorganic particles, remains intact under elevated temperature. The loading rate of fibrillated nonwoven reaches 23.2%, which is much higher than that on pristine nonwoven (10.4%).

Apart from loading capacity, the tight adhesion between carrier and catalyst constitutes another essential condition for practical applications, for it determines the durability of final products. Here two methods were adopted to respectively examine the dry and wet adhesion fastness of $CuO\text{-}CeO_2$ on fibrillated nonwoven, *i.e.* air blowing at 5 $m{\cdot}s^{-1}$ for 10 min, and washing under 1000 rpm for 10 min. It can be seen from Figure 3d (see also Video S1) that during the continuous air blowing, no particles are detected downstream of the filter. Also, neither the nonwoven nor the water changes color after washing (Figure 3e, see also Video S2). In accordance to these observations, the nonwoven exhibits no change of weight after repeated air blowing and washing (Figure S14), proving that $CuO\text{-}CeO_2$ particles are firmly attached on the fibrillated nonwoven under both dry and wet states. Reason for such a tight adhesion can be traced to the reaction mechanism of fibrillation (Figure 3f). Under the attack of electrophilic reagents (such as Lewis acid), the amide groups (acting as electron-donating groups) of para-aramid molecules help produce hydroxyl groups by improving the activity of phenyl ring ortho-para-reaction. Meanwhile, a small proportion of para-aramid molecular chain is hydrolyzed in H_3PO_4 solution, producing amino and carboxyl groups at both ends of the molecular chain. These active groups, together with the -P-OH groups grafted on fiber surface, form hydrogen bonds with the surface hydroxyl (OH) groups on $CuO\text{-}CeO_2$ (Figure 3g).[62-65] This mechanism is supported by Raman, Fourier transform infrared spectroscopy (FT-IR) and XPS spectra (Figure S15), and the decrease of water contact angle (WCA) from 151° to 130° (Figure S16) after fibrillation is also associated with the increase of hydroxyl groups (Ar-OH, -P-OH, -COOH).

View Article Online
DOI: 10.1039/D0TA07886G

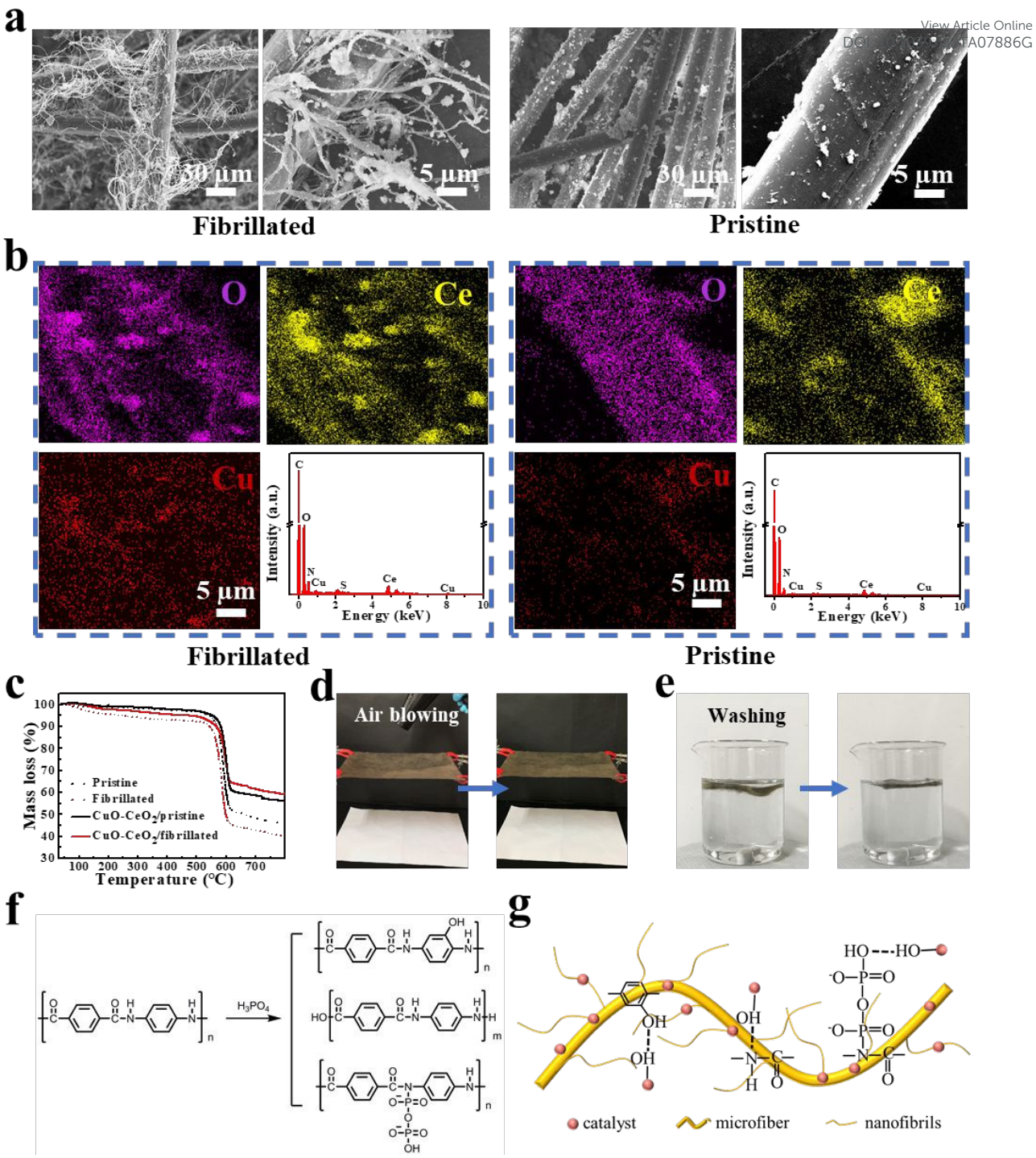

Figure 3. (a) SEM images of CuO-CeO_2 on fibrillated and pristine para-aramid nonwovens, (b) EDX mapping images of O, Ce, and Cu on fibrillated and pristine fibers, and EDS spectrum of CuO-CeO_2 on fibrillated and pristine para-aramid nonwovens. (c) TGA of fibrillated and pristine nonwovens with CuO-CeO_2. (d) Dry and (e) wet adhesion fastness of CuO-CeO_2 particles on fibrillated nonwovens. (f) Reactions of treating para-aramid fibers with H_3PO_4 solution and (g) the hydrogen-bonding interactions between CuO-CeO_2 and fibrillated para-aramid nonwoven.

The CuO-CeO_2/fibrillated nonwoven was then subjected to air filtration and CO conversion tests to evaluate its application potential as multifunctional air filter. With the adhesion of CuO-CeO_2, filtration performances of the nonwovens are further improved (Figure 4a), which can be explained by the combined effects of smaller pore size and larger SSA (Figure 4b). The filtration efficiency and QF of CuO-CeO_2/fibrillated nonwoven are 86.1% and 0.533 Pa^{-1}. According to the European Standard of Medium Efficiency Filters (BS EN 779: 2012), these values substantially surpass the requirements for medium efficiency filters. Furthermore, loading of abundant CuO-CeO_2 with high oxidative activity provides the fibrillated nonwoven with an excellent conversion capacity against CO. The complete

View Article Online
DOI: 10.1039/D0TA07886G

conversion temperature (~90 ℃) is much lower than that of the CuO-CeO_2/pristine nonwoven (~120 ℃, Figure 4c). By contrast, para-aramid nonwovens without catalysts, whether fibrillated or not, show no conversion of CO (Figure S17).

Besides converting CO under elevated temperature, the CuO-CeO_2/fibrillated nonwoven also exhibits a remarkable photodegradation capacity to VOCs under room temperature. Taking C_7H_8 as example, the nonwoven is able to degrade C_7H_8 in a short period. As shown in Figure 4d, more than 50% of the C_7H_8 can be removed within 1 h, and the complete removal is achieved in 6 h. Accompanied by the degradation of C_7H_8, the concentration of carbon dioxide (CO_2) increases synchronously (Figure S18), reflecting the successful conversion of C_7H_8 into CO_2 and H_2O. Given that CO is one of the major pollutants in automobile exhausts, and C_7H_8 is commonly distributed in indoor air, these results clearly suggest the efficacy and versatility of CuO-CeO_2/fibrillated nonwoven in purifying different types of air pollutants.

Thermal and chemical stabilities of para-aramid nonwoven are further strengthened by the adhesion of CuO-CeO_2 particles. As demonstrated in Figure 4e (see also video S3 and S4), all the samples would not be ignited due to the flame-retardant nature of para-aramid, and the CuO-CeO_2/fibrillated nonwoven suffers less decomposition than pure nonwoven. The abundant inorganic particles also keep the filtration performances of fibrillated nonwoven at a high level, even when immersing the nonwoven in 98% formic acid (HCOOH) solution and 0.5 mol·L^{-1} of sodium hydroxide (NaOH) solution for 1 h, respectively (Figure 4f).

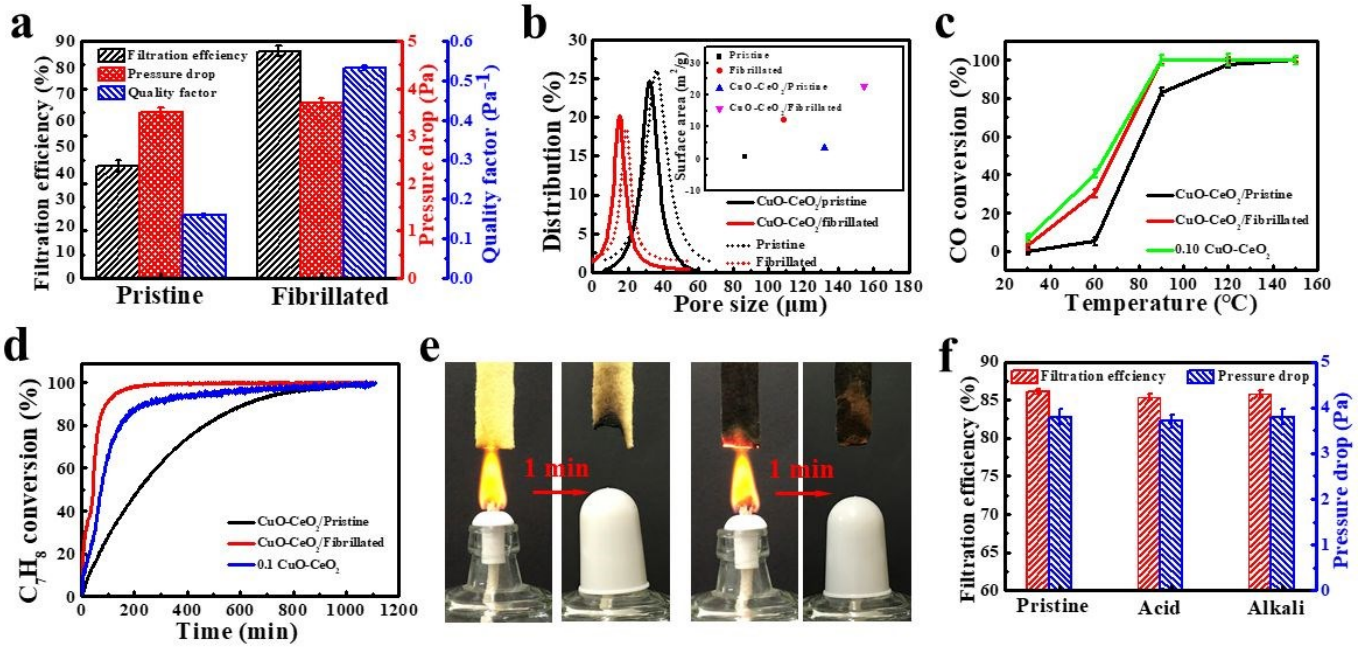

Figure 4. (a) Filtration performances, (b) pore size distribution and SSA, (c) CO conversion rate, and (d) C_7H_8 photocatalytic rate of pristine and fibrillated para-aramid nonwovens loaded with CuO-CeO_2. (e) Combustion behavior of fibrillated nonwovens with and without CuO-CeO_2. (f) Filtration performances of CuO-CeO_2/fibrillated nonwovens after 1 h of acid or alkali treatment.

When it comes to practical use, it is essential to scale up the production. Our strategy entails the manufacture of nonwoven (which is completely based on an industrialized process) as first step, and the fibrillation of fibers (which is achieved by simply treating the nonwoven with H_3PO_4 solution) as second step. Neither of these steps requires sophisticated equipment or tedious procedures. As a proof of scalable production, we prepared a roll of CuO-CeO_2/fibrillated nonwoven with a length of 180 cm and a working width of 40 cm (Figure S19). More attractively, it has been documented that a number of widely-adopted fibers, including cellulose fibers,[66-67] segmented-pie fibers[68-69] and polytetrafluoroethylene (PTFE) fibers,[70] possess similar fibrillation behaviors, and the fibrillated fibers have been reported as promising building blocks for separator of solid electrolytic capacitor,[71-72] orodispersible film,[73] healthcare,[74] and breathable apparels.[75] The nonwoven-based fibrillation strategy proposed in this study may be extended to a lot of materials and applications.

Conclusions

In summary, we have demonstrated the fabrication of nonwoven containing both microfibers and nanofibrils through exploiting the fibrillation behavior of para-aramid microfibers. With microfibers serving as the framework, the fibrillated nonwoven exhibits a stable 3D structure, while the presence of numerous nanofibers greatly reduces the pore size and enlarges the surface area. These features greatly improve the filtration efficiency of nonwoven without increasing the filtration resistance. Furthermore, when loaded with catalysts such as CuO-CeO_2, the fibrillated nonwoven possesses an enhanced loading capacity, and thus enabling the sufficient removal of both solid particles and toxic gases.

Conflicts of interest

There are no conflicts to declare.

View Article Online
DOI: 10.1039/D0TA07886G

Acknowledgements

This work was financially supported by the Fundamental Research Funds for the Central Universities (2232019G-01) and Graduate Student Innovation Fund of Donghua University (CUSF-DH-D-2020021).

Notes and references

1 G. Q. Gu, C. B. Han, C. X. Lu, C. He, T. Jiang, Z. L. Gao, C. J. Li and Z. L. Wang, *ACS Nano,* 2017, **11**, 6211-6217.
2 A. Kontses, A. Dimaratos, C. Keramidas, R. Williams, H. Hamje, L. Ntziachristos, and Z. Samaras, *Fuel,* 2019, **255**, 115879.
3 V. Kadam, I. L. Kyratzis, Y. B. Truong, J. Schutz, L. Wang and R. Padhye, *Sep. Purif. Technol.,* 2019, **224**, 247-254.
4 Z. Zhang, B. Dong, S. Li, G. Chen, Z. Yang, Y. Dong, Z. Wang, Y. Guo and J. Ma, *Sci. Total Environ.,* 2019, **691**, 868-873.
5 H. Qiu, L. Tian, K. F. Ho, V. C. Pun, X. Wang and I. T. Yu, *Environ. Pollut.,* 2015, **199**, 192-7.
6 R. Al-Attabi, Y. Morsi, W. Kujawski, L. Kong, J. A. Schütz and L. F. Dumée, *Sep. Purif. Technol.,* 2019, **215**, 500-507.
7 L.Zhang, W. Yuan, Z. Zhang, G. Zhang, H.Chen, N. Zhao, L. He and G. Tao, *J. Mater.Chem. A,* 2019, **7**, 4619-4625.
8 X. Fan, Y. Wang, M. Zheng, F. Dunne, T. Liu, X. Fu, L. Kong, S. Pan and W. Zhong, *J. Mater.Chem. A,* 2018, **6**, 21585-21595.
9 K. S. Han, S. Lee, M. Kim, P. Park, M. H. Lee and J. Nah, *Adv. Funct. Mater.,* 2019, 1903633.
10 J. Zhou and H. Wang, *Chem. Eng. J.,* 2020, **390**, 124567.
11 P. M. Rastogi, N.Kumar, A. Sharma, D.Vyas and A. Gajbhiye, *Pollution*, 2020, **6**, 25.
12 Z. Ren, V. Botu, S. Wang, Y. Meng, W. Song, Y. Guo, R. Ramprasad, S. L. Suib and P. X. Gao, *Angew. Chem. Int. Ed.,* 2014, **53**, 7223-7.
13 T. Yang, P. Zhang, B. Xu and J. Xiong, *Int. J. Heat Mass Transfer.,* 2017, **110**, 671-679.
14 K. J. Heo, J. W. Noh, B. U. Lee, Y. Kim and J. H. Jung, *Build. Environ.,* 2019, **161**, 106272.
15 L. Wang, Y. Kang, C. Y. Xing, K. Guo, X. Q. Zhang, L. S. Ding, S. Zhang and B. J. Li, *J. Hazard. Mater.,* 2019, **373**, 197-203.
16 J. Liu, H. Zhang, H. Gong, X. Zhang, Y. Wang and X. Jin, *ACS Appl. Mater. Interfaces,* 2019, **11**, 40592-40601.
17 T. T. Li, X. Cen, H. T. Ren, F. Sun, Q. Lin, C. W. Lou and J. H. Lin, *Polymers (Basel),* 2019, **11**.
18 P. Dixit, S. M. Ishtiaque and R. Roy, *Compos. B: Eng.,* 2020, **182**, 107654.
19 H. Zhang, J. Liu, X. Zhang, C. Huang and X. Jin, *J. Appl. Polym.Sci.,* 2018, **135**, 45948.
20 J. Liu, X. Zhang, H. Zhang, L. Zheng, C. Huang, H. Wu, R. Wang and X. Jin, *RSC Adv.,* 2017, **7**, 43879-43887.
21 S. Zhang, H. Liu, J. Yu, W. Luo and B. Ding, *J. Mater. Chem. A,* 2016, **4**, 6149-6157.
22 S. Zhang, H. Liu, N. Tang, J. Ge, J. Yu and B. Ding, *Nat. Commun.,* 2019, **10**, 1458.
23 M. Burgard, D. Weiss, K. Kreger, H. Schmalz, S. Agarwal, H.-W. Schmidt and A. Greiner, *Adv. Funct. Mater.,* 2019, **29**.
24 J. J. Huang, Y. Tian, R. Wang, M. Tian and Y. Liao, *Sep. Purif. Technol.,* 2020, **237**.
25 B. Ren, J. Liu, W. Huo, K. Gan, S. Yan, Y. Chen, Y. Lu, J. Yang and Y. Huang, *J. Am. Ceram. Soc.,* 2019, **102**, 2977-2986.
26 J. Liu, B. Ren, Y. Wang, Y. Lu, L. Wang, Y. Chen, J. Yang and Y. Huang, *Chem. Eng. J.,* 2019, **362**, 504-512.
27 S. Zhang, H. Liu, N. Tang, N. Ali, J. Yu, and B. Ding, *ACS Nano,* 2019.
28 H. Liu, S. Zhang, L. Liu, J. Yu and B. Ding, *Adv. Funct. Mater.,* 2019, **29**, 1904108.
29 J. Wang, S. Chen, W. Tang, Y. Dang, P. Kerns, R. Miao, B. Dutta, P. Gao and S. L. Suib, *Appl. Catal. B-Environ.,* 2019, **255**, 117766.
30 Y. Si, J. Yu, X. Tang, J. Ge and B. Ding, *Nat. Commun.,* 2014, **5**, 5802.
31 Y. A. May, W.-W. Wang, H. Yan, S. Wei and C. J. Jia, *Chinese J. Catal.,* 2020, **41**, 1017-1027.
32 X. Yang, Y. Pu, S. Li, X. Liu, Z. Wang, D. Yuan and X. Ning, *ACS Appl. Mater. Interfaces,* 2019, **11**, 43188-43199.
33 A. J. Binder,. T. J. Toops,. R. R. Unocic, J. E. Parks II, S. Dai, *Angew. Chem. Int. Ed.* 2015, **53**, 13263.
34 C. Xie, L. He, Y. Shi, Z. Guo, T. Qiu, X.Tuo, *ACS Nano,* 2019, **13**, 7811.
35 Z. Lu, L. Si, W. Dang and Y. Zhao, *Compo. Part A: Appl. Sci. Manuf.,* 2018, **115**, 321-330.
36 J. Wei, Y. Zhou, Y. Lv, J. Wang, C. Jia, J. Liu, X. Zhang, J. Sun and Z. Shao, *ACS Sustain. Chem. Eng.,* 2019, **7**, 12887-12896.
37 K. S. Salem, H. R. Starkey, L. Pal, L. Lucia and H. Jameel, *ACS Sustain. Chem. Eng.,* 2019, **8**, 1471-1478.
38 Z. Ma, S. Kang, J. Ma, L. Shao, A. Wei, C. Liang, J. Gu, B. Yang, D. Dong, L. Wei and Z. Ji, *ACS Nano,* 2019, **13**, 7578-7590.
39 F. Xie, F. Jia, L. Zhuo, Z. Lu, L. Si, J. Huang, M. Zhang and Q. Ma, *Nanoscale,* 2019, **11**, 23382-23391.
40 B. Yang, M. Zhang, Z. Lu, J. Tan, J. Luo, S. Song, X. Ding, L. Wang, P. Lu and Q. Zhang, *Carbohydr. Polym.,* 2019, **208**, 372-381.
41 H. Souzandeh, K. S. Johnson, Y. Wang, K. Bhamidipaty and W. H. Zhong, *ACS Appl. Mater. Interfaces,* 2016, **8**, 20023-31.
42 Z. Heng, Q. Xiao, Z. Qi and Y. Zhao, *J. Ind. Text.,* 2014, **45**, 48-65.
43 B. Y. Yeom and B. Pourdeyhimi, *J. Mater. Sci.,* 2011, **46**, 5761-5767.
44 Z. Dai, J. Su, X. Zhu, K. Xu, J. Zhu, C. Huang and Q. Ke, *J. Mater.Chem. A,* 2018, **6**, 14856-14866.
45 C. Zhang, L. Yao, Z. Yang, E. S.-W. Kong, X. Zhu and Y. Zhang, *ACS Appl. Nano Mater.,* 2019, **2**, 3916-3924.
46 H. Zhang, J. Liu, X. Zhang, C. Huang, Y. Zhang, Y. Fu and X. Jin, *J. Appl. Polym. Sci.,* 2019, **136**, 47827.
47 K. Feng, B. Song, X. Li, F. Liao and J. Gong, *Ecotoxicol Environ. Saf.,* 2019, **171**, 587-593.
48 Y. Guo, Y. Gao, X. Li, G. Zhuang, K. Wang, Y. Zheng, D. Sun, J. Huang and Q. Li, *Chem. Eng. J.,* 2019, **362**, 41-52.
49 E. Moretti, L. Storaro, A. Talon, M. Lenarda, P. Riello, R. Frattini, M. d. V. M. de Yuso, A. Jiménez-López, E. Rodríguez-Castellón, F. Ternero, A. Caballero and J. P. Holgado, *Appl. Catal. B,* 2011, **102**, 627-637.
50 C. Y. Chaparro-Garnica, A. Davo-Quinonero, E. Bailon-Garcia, D. Lozano-Castello and A. Bueno-Lopez, *ACS Appl. Mater. Interfaces,* 2019, **11**, 36763-36773.
51 J. Lu, J. Wang, Q. Zou, Y. Zhao, J. Fang, S. He, D. He and Y. Luo, *J. Alloys. Compd.,* 2019, **784**, 1248-1260.
52 H. Liu, Z. Fan, C. Sun, S. Yu, S. Feng, W. Chen, D. Chen, C. Tang, F. Gao and L. Dong, *Appl. Catal.B,* 2019, **244**, 671-683.
53 Y. Xie, J. Wu, G. Jing, H. Zhang, S. Zeng, X. Tian, X. Zou, J. Wen, H. Su, C. J. Zhong and P. Cui, *Appl. Catal. B,* 2018, **239**, 665-676.
54 G. Avgouropoulos and T. Ioannides, *Appl. Catal. A: Gen.,* 2003, **244**, 155-167.
55 S. Zeng, Y. Wang, S. Ding, J. J. H. B. Sattler, E. Borodina, L. Zhang, B. M. Weckhuysen and H. Su, *J. Power Sources,* 2014, **256**, 301-311.
56 W.Liu and M. F. Stephznopoulos, *J. Catal.* 1995, **153**, 304-316.
57 H. Yen, Y. Seo, S. Kaliaguine and F. Kleitz, *Angew. Chem. Int. Ed.,* 2012, **51**, 12032-5.
58 X. Wang, Y. Liu and Z. Wu, *Chem. Eng. J.,* 2020, **382**, 122941.
59 X. Guo, Z. Qiu, J. Mao and R. Zhou, *J. Power Sources,* 2020, **451**, 227757.
60 Y. Zeng, Y. Wang, F. Song, S. Zhang and Q. Zhong, *Sci. Total Environ.,* 2020, **712**, 135635.
61 X. Zhang, G. Li, R. Tian, W. Feng and L. Wen, *J. Alloys Compd.,* 2020, **826**, 154149.
62 W. Wang, Z. Qu, L. Song and Q. Fu, *J. Energy Chem.,* 2020, **40**, 22-30.
63 Y. Zhao, D. Chen, J. Liu, D. He, X. Cao, C. Han, J. Lu and Y. Luo, *Chem. Eng. J.,* 2020, **389**, 124384.

View Article Online
DOI: 10.1039/D0TA07886G

64 T. V. Plakhova, A. Y. Romanchuk, S. M. Butorin, A. D. Konyukhova, A. V. Egorov, A. A. Shiryaev, A. E. Baranchikov, P. V. Dorovatovskii, T. Huthwelker, E. Gerber, S. Bauters, M. M. Sozarukova, A. C. Scheinost, V. K. Ivanov, S. N. Kalmykov and K. O. Kvashnina, *Nanoscale,* 2019, **11**, 18142-18149.
65 Z. Liu, E. Huang, I. Orozco, W. J. Liao, R. M. Palomino, N. Rui, T. Duchon, S. Nemsak, D. C. Grinter, M. Mahapatra, P. Liu, J. A. Rodriguez and S. D. Senanayake, *Science,* 2020, **368**, 513..
66 Y. Ren, B. R. Linter and T. J. Foster, *Food Hydrocoll.,* 2020, **104**, 105725.
67 V. Kumar, P. Pathak and N. K. Bhardwaj, *Carbohydr. Polym.,* 2020, **238**, 116186.
68 H. Zhang, X. Qian, Q. Zhen and Z. Yang, *J. Ind. Text.,* 2015, **45**, 48-65.
69 A. Durany, N. Anantharamaiah and B. Pourdeyhimi, *J. Mater. Sci.,* 2009, **44**, 5926-5934.
70 T.-W. Shyr, W.-C. Chung, W.-L. Lu and A.-J. Lin, *Eur. Polym. J.,* 2015, **72**, 50-63.
71 T. Shigematsu (Mitsubishi Paper Mills Ltd) *JP2020053425-A*, 2020**.**
72 Y. Wang, J. Long, J. Hu, Z. Sun and L. Meng, *J. Power Sources,* 2020, **453**, 227853.
73 V. Lenhart, J. Quodbach and P. Kleinebudde, *Aaps Pharmscitech.,* 2019, **21**.
74 P. Jingjit and N. Srisawat, *J. Nanosci. Nanotechnol.,* 2019, **19**, 1554-1561.
75 B. Zhao, X. Qian, Y. Qian, Y. Duo, Y. Feng, J. Fan, and Y. Chen, *AATCC J. Res.,* 2019, **6**, 45-49.

View Article Online
DOI: 10.1039/D0TA07886G

Graphical abstract

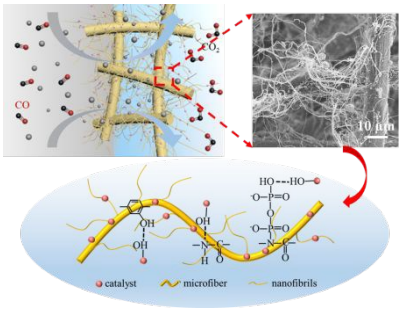

Para-aramid nonwoven composed of both micro- and nanofibers is loaded with CuO-CeO_2 to remove solid and gaseous pollutants.